Enabling and Boosting Preferential Epitaxial Zinc Growth via Multi-Interface Regulation for Stable and Dendrite-free Zinc Metal Batteries

Yangyang Wang, Tiantian Ren, Zeping Wang, Chengxin Liu, Yuhang Zhang, Ao Xu, Chunxia Chen, Jinbo Bai, Hui Wang, Xiaojie Liu

Enabling and Boosting Preferential Epitaxial Zinc Growth via Multi-Interface Regulation for Stable and Dendrite-free Zinc Metal Batteries

Yangyang Wang[1], Tiantian Ren[1], Zeping Wang[1], Chengxin Liu[1], Yuhang Zhang[1], Ao Xu[1], Chunxia Chen[1], Jinbo Bai[2], Hui Wang[1] and Xiaojie Liu[1]*

[1] *Key Laboratory of Synthetic and Natural Functional Molecule of the Ministry of Education, College of Chemistry & Materials Science, Northwest University, Xi'an 710127, P. R. China*

[2] *Laboratoire Mécanique des Sols, Structures et Matériaux (MSSMat), CNRS UMR 8579, Ecole CentraleSupélec, Université Paris-Saclay, 8-10 rue Joliot-Curie, 91190 Gif-sur-Yvette, France*

* Corresponding Author:

E-mail address: xiaojie.liu@nwu.edu.cn (X. Liu)

Abstract:

The practical application of aqueous Zn-metal anodes (AZMAs) is mainly impeded by the short cycling life and unsatisfactory reversibility springing from the notorious Zn dendrite growth and detrimental water-induced parasitic reactions at anode-electrolyte interface. To tackle these challenges, a multifunctional interface of Sn-modified $Ti_3C_2Cl_2$ MXene (denoted as Sn-MXene) with high zincophilic and hydrophobic property is rationally designed via a one-step strategy with a novel molten salt etching to achieve dendrite-free Zn deposition. Experimental results and theoretical calculations reveal that the Sn nanoparticles can induces a strongly zincophilic surface with high Zn^{2+} adsorption, and the $Ti_3C_2Cl_2$ MXene significantly decreases the surface energy of the Zn (002) plane, guiding the zinc preferred orientation along the (002) plane in electroplating growth process. Moreover, the hydrophobic properties of -Cl terminations of protective interface for the Zn anode can regulate Zn-ion solvation structure to mitigate H_2O-decomposition-induced side reactions, and guaranteeing a steady stream of Zn^{2+} flux. Encouragingly, benefiting from the Sn-MXene layer, a side reaction-free and dendrite-free Zn anode with an excellent lifespan is achieved, which is further applied as an anode for full battery (Sn-MXene-Zn//α-MnO_2) with a long-term span over 800 cycles under 1 A g^{-1} with a capacity retention of 96%.

Keywords: Zn anode; Sn-modified $Ti_3C_2Cl_2$ MXene; Hydrophobic; Controllable deposition; Multi-interface regulation

1. Introduction

Low price, intrinsic safety, environmental-friendly and convenient assembly rechargeable aqueous Zn-ion batteries (AZIBs) have nowadays been recognized as a reliable contender for grid-scale energy systems.[1] Metallic Zn exhibits numerous appealing features in aqueous batteries, including high theoretical capacity (5855 mAh cm^3 or 820 mAh g^{-1}) and appropriate low redox potential (–0.762 V vs. the standard hydrogen electrode), as well as rich crustal reserves.[2] Nevertheless, the critical issues including uncontrolled Zn dendrite growth, harmful parasitic reactions and irreversible by-products are the culprits of disappointing electrochemical reversibility and low utilization ratio of metallic Zn, which further induces severe capacity fading of the cells during cycling and has become major obstacles to the widespread commercialization of AZIBs. Furthermore, the hydrogen evolution reaction (HER) occurs easily in aqueous environment resulting from the larger standard electrode potential value (0 V vs. SHE) in comparison with the potential of Zn^{2+}/Zn.[3] Meanwhile, the persistent H^+ depletion in electrolyte caused by HER not only results in an increase in local pH to produce the undesirable accumulation of insulating by-products of $Zn(OH)_2$ and ZnO, and zinc corrosion at the Zn anode/electrolyte interface, but also brings about the formation of an inactive passivation layers $Zn_4SO_4(OH)_6 \cdot xH_2O$ (x=1–6), thereby severely reducing CE and battery life.[4]

To overcome above-mentioned challenges faced by Zn anodes, the construction of artificial protective layers (APLs) as interface regulation have been deemed one of the most effective methods adopted in mild acidic electrolyte to block direct contact between the electrolyte and Zn anode due to the thermodynamic instability of metal zinc in acidic medium.[5] They typically act as ion screens to filtrate the ions that pass through the coating, hinging on their elaborately tailored aperture. Additionally, an effective surface regulation can transfer surface charges at a high rate and generate uniform interfacial electric fields near the anode during zinc deposition, thus retarding side reactions and impeding Zn dendrite formation. Among various APLs materials,

zincophilic species, such as Au,[6] Cu,[7] TiO_2,[8] Ag,[9] have been commonly investigated in regulating zinc metal. On the one hand, the zincophilic species could not only act as heterogeneous seeds but also effectively optimize the distributed electric fields to guide dendrite-free Zn deposition. On the other hand, they can minimize the Zn nucleation overpotential and reduce the HER. Impressively, the highly zincophilic metallic Sn can deliver a strong Zn^{2+} adsorption, which is critical for regulating nucleation and uniform deposition of Zn. Specifically, the Sn layer endows the anode with distinct advantages: (i) the high-affinity zinc-binding sites of Sn affords low energy barrier of deposition;[10] (ii) the Sn element strengthens the interaction between H and O atoms, thus enhancing the HER barrier;[11] (iii) the Sn layer greatly retards water-induced side reactions.[12] While, so far metallic Sn species has not yet investigated deeply, and the underlying value of Sn on enhancing Zn^{2+} diffusion has not yet been determined. Beyond that, it is worth noting that traditional APLs merely focused on their role in eliminating the water-induced side reactions and simultaneously homogenizing the flux of Zn^{2+}, thus enhancing the cyclicity of Zn electrodes to a certain extent, while their potential effect on influencing the Zn preferential growth of repetitive Zn deposition/dissolution was ignored, which hinders the further advancement of AZIBs. Considering that the growth direction of the newly deposited metal is induced by the crystallographic orientation of the electrode, it is implied that the crystal homogeneity of the metal electrode evolves into the uniformity of the deposited metal morphology.[13] Therefore, the surface crystal uniformity of the metal electrode can regulate long-term planar and dendrite-free Zn plating/stripping. Specifically, Zn is a typical hexagonal close-packed (hcp) structure including the (002), (101), and (100) crystal planes with large relative texture coefficients (RTCs).[1e] The final morphology of zinc deposition can be determined by the preferred crystal plane. Currently, it has been recognized that the surface of the Zn (002) crystal plane has relatively smoother surface atom arrangement in contrast with Zn (100) and (101) crystalline surfaces and exhibits a more even interface charge density, which tends to deposit horizontally to inhibit the production of zinc dendrites,

thus elevating the cyclability of Zn anodes.[14] Moreover, due to its low surface energy, more exposed Zn (002) surfaces can somewhat offer a stronger ability against corrosion and H_2 production.[15] Up to now, electrolyte optimization is a common method to enhance the stability of Zn anode by introducing additives to manipulate Zn (002) crystal orientation in AZIBs, which is highly attractive due to its convenience and cost effectiveness.[1e, 16] Nevertheless, there are relatively few studies on the preferential growth for specific Zn (002) crystal plane induced by Zn surface regulation. In consequence, it is necessary to develop the artificial protective layers with preferred Zn (002) textured deposition, acting with metallic Sn synergically, to implement multi-interface regulation on Zn metal.

Transition metal carbides or/and nitrides (MXene), a rising star of two-dimensional (2D) transition metal, has been considered as a boon as high-rate electrode materials for supercapacitors and rechargeable batteries.[17] Benefiting from the unique 2D layered structure including metallic-level conductivity, tunable surface terminations and structural variety with excellent mechanical strength, MXene-based coating materials can effectively induce uniform Zn^{2+} deposition as artificial layers.[18] It is noteworthy that $Ti_3C_2T_x$ MXene has a low lattice mismatch rate (about 10%) with zinc metal, implying its promising potential for orientating and promoting preferential zinc growth along Zn (002). To be specific, a negative value of adsorption energy for $Ti_3C_2T_x$ MXene indicates the inherent affinity of MXene for Zn. The modification of zinc anodes with $Ti_3C_2T_x$ MXene results in a low adsorption energy, enabling uniform deposition of zinc ions parallel to the (002) base surface and facilitating horizontal growth of the Zn (002) surface during subsequent cycles, thereby inhibiting the formation of dendrites. Although $Ti_3C_2T_x$ MXene is an ideal protection material for zinc anode, the mechanism by which $Ti_3C_2T_x$ MXene layer regulates the texture growth of zinc metal is yet to be elucidated; thus, further research is highly required. As a result, based on the distinctive features of metallic Sn and 2D MXene, it is highly believed that the integrity of Sn and $Ti_3C_2T_x$ MXene can enable a stable and dendrite-free Zn deposition via the multi-interface regulation, particularly orientating

and boosting preferential epitaxial zinc growth of (002) plane. In addition, MXenes have conventionally been prepared by selective etching approaches introducing fluoride-containing acidic solutions, which inevitably raises safety concerns and limits its large-scale preparation.[19] The conventional F-MXene created through such strategies has poor modulation ability for the zinc anode, which shows non-uniform distributed current density and Zn^{2+} flux concentrated at "hot spots". Recently, by a brand-new strategy for MXenes (i.e. Lewis acidic etching), the hierarchical structure of Sn and $Ti_3C_2T_x$ MXene can be achieved simultaneously, thereby providing multifunctionality to the Zn anodes.

In this work, a mechanically strong, zincophilic and hydrophobic $Ti_3C_2Cl_2$ MXene with the modification of Sn (denoted as Sn-MXene) is proposed as a multifunctional coating on Zn anode surface, which is prepared by etching MAX Ti_3AlC_2 in molten $SnCl_2$ salt at 600 ℃ (Figure 1a). The approach can allow unprecedented control over the surface chemistry, structure and properties of MXene. $Ti_3C_2Cl_2$ MXene manipulates Zn^{2+} deposition on MXene matrixes by means of tiling rather than stacking, indicating that a high lattice matching between MXene and Zn and the establishment of coherent heterogeneous interface to regulate subsequent Zn^{2+} ion deposition. To ensure uniform Zn stripping/plating and accelerate Zn^{2+} migration, the Zn electrode modified by Sn-MXene (Sn-MXene-Zn) exhibits distinctive merits (Figure 1b): i) The accordion-like Sn-MXene efficiently provides transport channels for Zn^{2+} migration and enhances the diffusion kinetics of Zn^{2+}. ii) The zincophilic Sn supplies low nucleation overpotential, excellent Zn affinity and high conductivity. iii) The electronegative -Cl terminations in Sn-MXene functionalize as ion motors to be hydrophobic and extract Zn^{2+} from the hydrated species of $[Zn(H_2O)_6]^{2+}$ and further speed up the transport of diffused Zn^{2+}. iv) The electronegative -Cl terminations show strong interaction with Zn atoms, resulting in a lower surface energy in the Zn (002) planes. The zincophilic interplay between Sn-MXene and the underlying Zn substrate significantly reduces the surface energy of the Zn (002) crystal plane, which induces the preferred orientation of Zn dendrites along the (002) crystal plane. Benefiting

from these advantages, the Sn-MXene-modified Zn anode (Sn-MXene-Zn) achieves high cycling stability, good reversibility and excellent electrochemical kinetics, which can cycle stably for 920 h at 5 mA cm^{-2}/5 mAh cm^{-2} in symmetric cell. When assembled with MnO_2 cathode into a full cell, it exhibits improved cyclability and extraordinary rate performance, indicating promising potential for practical application.

2. Results and Discussion

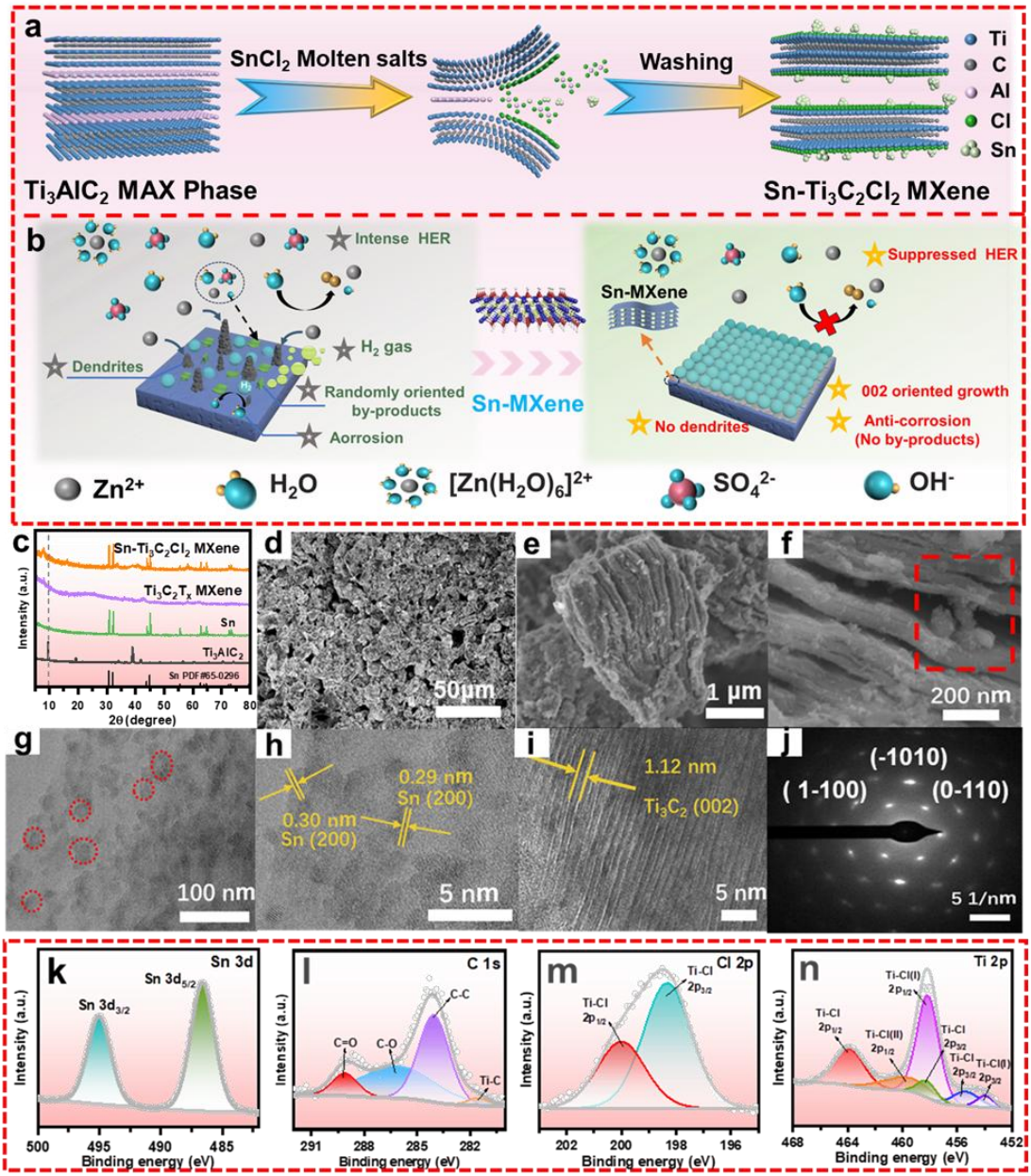

Figure 1. (a) Diagrams of the synthesis of Sn-MXene composites by $SnCl_2$ molten salt reaction. (b) Schematic illustrations of Zn metal plating behaviors on bare Zn and Sn-MXene-Zn electrodes. (c)

XRD patterns of Ti_3AlC_2, Sn, $Ti_3C_2T_x$ MXene and Sn-MXene. (d-f) SEM images of Sn-MXene. (g-j) TEM images and the SAED image of Sn-MXene. XPS spectra of (k) Sn 3d, (l) C 1s, (m) Cl 2p and (n) Ti 2p of Sn-MXene.

As schematically illustrated in Figure 1a, the multifunctional Sn-MXene composites was synthesized through a molten salt reaction method (for details, see Figure S1, Supporting Information), employing Ti_3AlC_2 MAX phase as the precursor and $SnCl_2$ as etchant according to the detailed reaction mechanism expressed as following equation:[20]

$$Ti_3AlC_2+SnCl_2 \rightarrow Ti_3C_2+AlCl_3 \uparrow +Sn \qquad \text{Equation (1)}$$

$$Ti_3C_2+SnCl_2 \rightarrow Ti_3C_2Cl_2+Sn \qquad \text{Equation (2)}$$

The X-ray diffraction (XRD) spectra explicitly reflects the structural changes during the $SnCl_2$ molten salt etching process (Figure 1c and Figure S2, Supporting Information). Different from the initial phase Ti_3AlC_2, the significant diffraction (104) peak at 39.8° disappears for Sn-MXene owing to the successful Al etching. Besides, the (002) peak of 9.49° (Ti_3AlC_2) shifts to a lower angel of 7.88° (Sn-MXene), demonstrating the successful preparation of layered structure of $Ti_3C_2Cl_2$ MXene. Meanwhile, the diffraction peaks corresponding to Sn nanoparticles could match well with the standard card (JCPDS # 65–0296).[10] In this way, Sn-nanoconfined $Ti_3C_2Cl_2$ MXene layered structures are successfully synthesized under the $SnCl_2$ molten salt reaction. In order to further explore the detailed microstructure of the Sn-MXene composites, scanning electron microscopy (SEM) and transmission electron microscope (TEM) are characterized (Figure 1d-j). The SEM images (Figure 1d-e) reveal Sn-MXene has the typical accordion like morphology with a lateral size of approximately 3-4 μm. As further characterized by TEM (Figure 1g-j), the Sn nanoparticles with Sn-MXene composites can be easily observed and lattice fringe can also be visible as marked by a yellow line, which is attributed to the (200) plane of metallic Sn.[21] The interlayer spacing of $Ti_3C_2Cl_2$ MXene is measured to be ≈ 1.12 nm for (002) plane in the high-resolution TEM (HRTEM) images,[17c] much larger

than the $Ti_3C_2T_x$ MXene obtained (≈ 0.98 nm) in agreement with the XRD pattern (Figure S3, Supporting Information). Meanwhile, the $Ti_3C_2T_x$ MXene retains the accordion-like structure. The SEM images of commercial Sn are shown in (Figure S4, Supporting Information). The corresponding selected area electron diffraction (SAED) pattern exhibits that the typical hexagonal symmetry of the planes, reflecting that the good crystallinity of the obtained Sn-MXene nanosheets. Besides, the homogeneous distributions of Ti, Cl, C and Sn elements throughout the Sn-MXene structure without segregation and residual precursors are clearly confirmed in both SEM and TEM of the energy-dispersive X-ray spectroscopy (EDS) mapping patterns observation (Figure S5, Supporting Information). As listed in Table S1, Supporting Information, the account of Sn element is 22.60 wt% in the Sn-MXene. Moreover, the chemical states of C, Ti and Cl elements in the Sn-MXene and MXene are verified by the high-resolution X-ray photoelectron spectroscopy (XPS) (Figure 1k-n and Figure S6-7, Supporting Information), which agrees well with the previous results.[22] In the high-resolution XPS Sn 3d spectra of Sn-MXene, the binding energies of 495.6 eV and 486.9 eV are assigned to the $3d_{3/2}$ and $3d_{5/2}$ orbitals of Sn, respectively,[23] further confirming the existence of Sn in the monomeric form in the Sn-MXene composites. Also, the Sn-MXene and $Ti_3C_2T_x$ MXene exhibit similar porosity with small surface areas (≈ 5.1 $m^2 g^{-1}$ for Sn-MXene and ≈ 4.6 $m^2 g^{-1}$ for the $Ti_3C_2T_x$ MXene) (Figure S8, Supporting Information), favorable for the rapid transport of electrolyte ions. The uniform and dense coating thickness of the Sn-MXene/PVDF powders is ≈ 8.1μm, as estimated by the cross-sectional SEM image. Besides, the EDS mappings of Sn-MXene-Zn is shown in Figure S9, Supporting Information, further revealing that C, Cl, Ti and Sn elements are evenly distributed on the zinc foil. Furthermore, Sn-MXene-Zn fabrication is prepared using an appropriate amount of viscous PVDF (10 wt.%) to ensure excellent adhesion and mechanical robustness between the Sn-MXene and Zn after the bending, folding and twisting tests (Figure S10, Supporting Information). Even after many times bending, folding and twisting tests, the Sn-MXene layer still

keeps intact on the surface of Zn foil without any visible cracks and peeling.

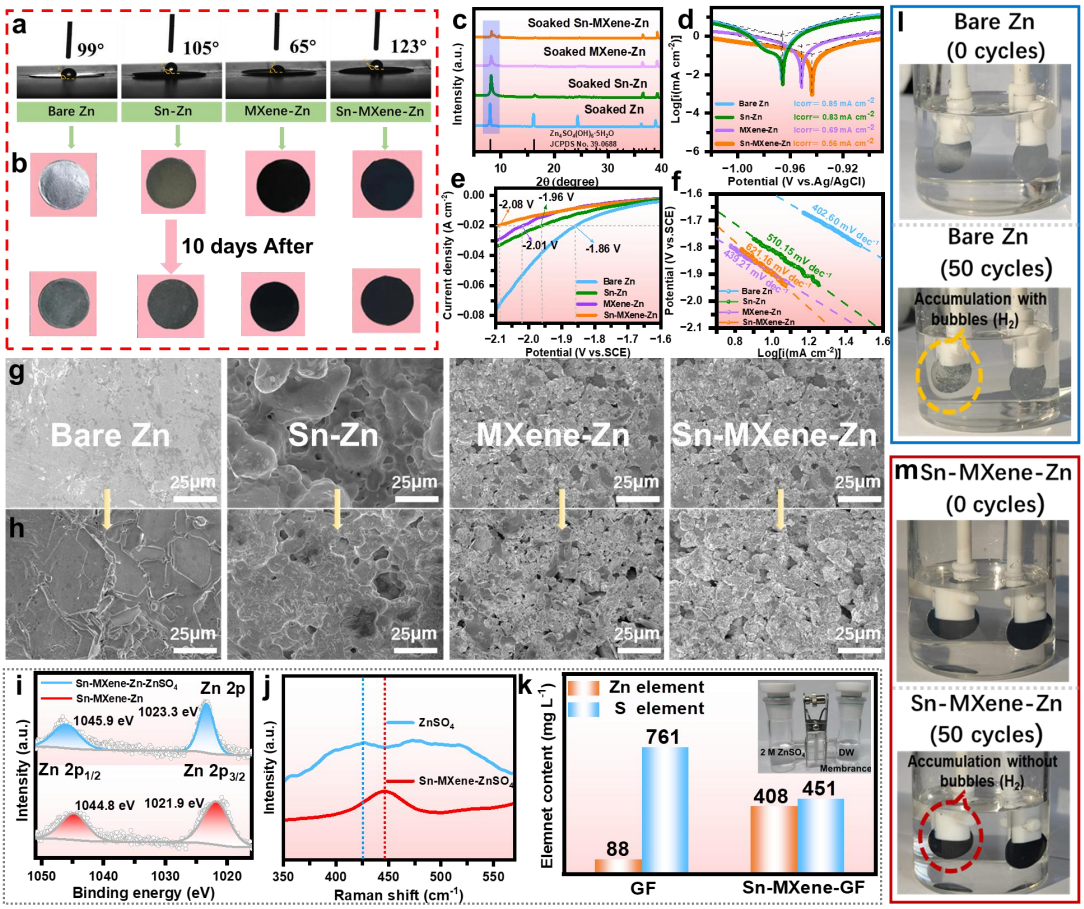

Figure 2. Side reaction resistance of Sn-MXene-Zn electrode. (a) Contact angles of 2 M $ZnSO_4$ aqueous solution on the different electrodes. (b) Digital photos of different electrodes in the initial state and after immersion in 2 M $ZnSO_4$ electrolyte for 10 days. (c) XRD patterns of different electrodes after immersion. (d) Corrosion, (e) HER curves and (f) the corresponding Tafel slopes of different electrodes. SEM images of different electrodes in the initial state (g) and after immersion (h) in 2 M $ZnSO_4$ electrolyte for 10 days. (i) Raman spectra of $ZnSO_4$ electrolyte and Sn-MXene–$ZnSO_4$ for v-SO_4^{2-} bond vibration. (j) XPS spectra of Zn 2p. The Sn-MXene layers before and after being immersed into 2 M $ZnSO_4$ electrolyte are noted as Sn-MXene-Zn and Sn-MXene-Zn–$ZnSO_4$, respectively. (k) Zn^{2+} and SO_4^{2-} permeability of GF and Sn-MXene-GF membrane (the inset: H-cell for ionic selectivity and permeability test). In situ optical microscopy observation of Zn deposition on zinc foils in (l) bare Zn and (m) Sn-MXene-Zn.

The notorious side reactions (HER and corrosion) on the zinc surface, as well as zinc deposition during the charging step, are essential causes of AZIBs failure.[14, 24] The wettability of bare Zn, Sn-Zn, MXene-Zn and Sn-MXene-Zn in a 2 M $ZnSO_4$ electrolyte is conducted with contact angle tests at ambient conditions (Figure 2a).

The contact angle of the MXene-Zn (65°) is smaller than that of the bare Zn (99°), but the Sn-MXene coating endows the zinc foil with more hydrophobic property with a contact angle of 123°, which mainly derives from Cl-terminated Sn-MXene with strong electronegativity and electric induction effect. This result confirms that hydrophobic groups are expected to significantly mitigate free water and dissolved oxygen inherent in $ZnSO_4$ electrolytes from contacting and corroding the active Zn surface when the Sn-MXene is used as an interfacial protective layer for zinc anode. Furthermore, the hydrophobic surface can alleviate the concentrated polarization of zinc ions and improve the stability of bare zinc electrodes. To further investigate the corrosion behavior of the zinc anodes, the prepared electrodes are immersed into 2 M $ZnSO_4$ solution for 10 days. As presented in Figure 2b, the surface of the soaked bare Zn becomes rough and completely loses its metallic luster after 10 days, indicative of its undesirable interfacial side reaction between the pristine Zn anode and $ZnSO_4$ solution. In comparison, with the protection of Sn and/or MXene, the other three soaked electrodes (Sn-Zn, MXene-Zn, and Sn-MXene-Zn) can basically remain their initial appearance without visible damage and color change on the surface, revealing that both Sn and MXene can effectively enhance anti-corrosive ability by isolating the interface between the Zn surface and the electrolyte. Several evident corrosion-product-related peaks at 8.3°, 16.3°, and 24.5° for XRD patterns belongs to $Zn_4SO_4(OH)_6{\cdot}5H_2O$ phase (JCPDS# 39-0688),[12] which is a typical byproduct of Zn. Figure 2c clearly shows that the intensity of the peaks corresponding to byproducts in soaked Sn-MXene-Zn is the weakest, confirming the drastic corrosion reactions are efficiently disrupted by the compact Sn-MXene layer. Additionally, the soaked XRD patterns displays that separate APL such as Sn and MXene layers cannot greatly prevent the formation of $Zn_4SO_4(OH)_6{\cdot}5H_2O$ on the surface of Zn as prolonged exposure to the water-based electrolyte is detrimental for the long-term cyclability of AZMAs. Moreover, the corresponding SEM images after immersion are depicted in Figure 2g-h, which is consistent with the XRD and photographs. In regard to commercial Zn plate, there is an obvious morphology change from a smooth and flat

surface to a messy surface attached with numerous hexagonal flake-like crystals. As anticipated, no obvious trace of corrosion is observed at the Sn-MXene-electrode after immersing, which again proves that the stable mechanical integrity and significant improved thermodynamic stability between the APL and Zn. Subsequently, the anti-corrosive effects of bare Zn, Sn-Zn, MXene-Zn, and Sn-MXene-Zn are further investigated through linear polarization measurements with three-electrode conditions (Figure 2d and Figure S11, Supporting Information). It can be observed that the Sn-MXene-Zn displays a lesser corrosion current density (I_{corr}, 0.56 mA cm^{-2}) and a higher corrosion potential (E_{corr}, –0.943 V) than bare Zn (0.85 mA cm^{-2} and –0.967 V), Sn-Zn (0.83 mA cm^{-2} and –0.965 V) and MXene-Zn (0.69 mA cm^{-2} and –0.951 V), which reflects strongly decreased corrosion rate and tendency, respectively, in the zinc sulfate electrolyte using multifunctional Sn-MXene interface. Experimental evidence for the restricted HER over Sn-MXene-Zn is acquired from linear sweep voltammetry (LSV) tests at a scan rate of 1 mV s^{-1} in three-electrode configurations, where a 1 M Na_2SO_4 solution (vs SCE) is employed to precisely analyze the HER kinetics to minimize the Faraday currents without the interference of Zn ion redox reaction. At the initial period of the electrochemical course, the current approaching zero before the beginning of HER in the LSV profiles (non-faradic area) is developed via the electric double layer capacitance instead of HER (Figure S12, Supporting Information).[25] Besides, the onset of HER is determined by the hydrogen evolution overpotential of H_2 according to the LSV curve. If the overpotential value can be diminished, a more distinct separation boundary can be developed between the Zn deposition course and HER. As shown in the LSV curves (Figure 2e), the V_{HER} values (vs SCE) increased in the order: Sn-MXene-Zn (–2.08 V) < MXene-Zn (–2.01 V) < Sn-Zn (–1.96 V) < bare Zn (–1.86 V), meaning the superior HER shielding effect of Sn-MXene-Zn. The Tafel slope (Figure 2f) of the Sn-MXene-Zn electrode (621.16 mV dec^{-1}) is higher than that of the bare Zn (402.60 mV dec^{-1}), Sn-Zn (510.15 mV dec^{-1}) and MXene-Zn (439.21 mV dec^{-1}), further confirming the sluggish HER rate endowed by multifunctional Sn-MXene interface. As displayed in Figure S13,

Supporting Information, a detection device consisting of a pH meter and a cuvette is developed, in which the $ZnSO_4$ electrolyte is added with 10 mL. Remarkably, Sn-MXene-Zn displays a more stable pH tendency during the cycle, in stark contrast to the exposed bare Zn, which shows a continuous rise as a result of the intimate contact of water. We also use the visualized transparent Zn–Zn symmetric batteries to observe the reaction phenomena on the Zn foil surface to analyze the positive effect of Sn-MXene layer on the HER at the electrolyte/zinc interface. There are plenty of zinc dendrites, "dead Zn" and bubbles accumulation (H_2) on the bare zinc foil surface after 50 cycles (Figure 2l). For Sn-MXene-Zn system, at the same condition, neither "dead zinc" nor bubbles on the Zn anode surface all throughout the test are visualized (Figure 2m). The above result intuitively reflects prominent corrosion resistance of Sn-MXene layer.

The Zn^{2+} transference number (t_{Zn}^{2+}) is measured by chronoamperometry (CA) and electrochemical impedance spectroscopy (EIS) analysis to quantitatively estimate Zn^{2+} transport facilitation capacity under Sn-MXene protection, which can be calculated by the Bruce-Vincent method (Equation S1, Supporting Information).[5b, 25b] As shown in Figure S14, Supporting Information, the value of t_{Zn}^{2+} increases remarkably from 0.44 in the bare Zn cell to 0.74 in the Sn-MXene-Zn cell, evidencing that the Sn-MXene layer can greatly expedite the transportation of Zn^{2+}, mitigate the interface concentration gradient between the Zn anode and electrolyte, and achieve homogeneous Zn plating/stripping, thereby suppressing the dendrite propagation. Besides, the ionic conductivity of the Sn-MXene interfacial layer is determined by EIS plots (Figure S15, Supporting Information), which displays a high ionic conductivity of 1.43×10^{-3} S cm^{-1} (Equation S2, Supporting Information).[25b] These results again demonstrate that Sn-MXene accelerates transport of Zn^{2+} and therefore improves ionic conductivity. In addition, as illustrated in Figure 2i, the solvated structure of Zn^{2+} is explored based on Raman spectroscopy. The peak at 426 cm^{-1} belongs to SO_4^{2-} shifts to a high frequency in the electrolyte added to Sn-MXene by the action of the contact ion pair Zn^{2+}–OSO_3^{2-} in contrast to the original $ZnSO_4$

electrolyte.[26] This indicates that the interaction between Sn-MXene and water molecules is stronger than between water and Zn^{2+}, which leads to the structural changes of Zn^{2+} solvent. The XPS is performed to examine the bonding state (Figure 2j). After soaking, the binding energy peak of Zn shifts to the left. Based on the Bader charge analysis, the change of Zn charge interacting with H_2O is positive, that is the increase of effective nuclear charge leads to the increase of binding energy,[27] indicating that Sn-MXene can interact with water consistent with the Raman tests results. Furthermore, the ionic permeability and selectivity of the APL composed of the Sn-MXene are performed by an H-cell test by separating the deionized water (DW) and 2 M $ZnSO_4$ electrolytes (Figure 2k).[28] Inductively coupled plasma (ICP) of the collected DW after 120 min of stirring show that a significantly higher concentration of Zn^{2+} ions in the Sn-MXene-GF separator cell (408 mg L^{-1}) than the pristine GF (88 mg L^{-1}). Similarly, the SO_4^{2-} concentration value of pristine GF separator is 761 mg L^{-1}, and it is distinct that using a Sn-MXene-GF separator can decrease the amount of SO_4^{2-} (451 mg L^{-1}).The above results demonstrate that the multi-interface regulation effect of Sn and $Ti_3C_2Cl_2$ MXene significantly could effectively promote Zn^{2+} diffusion and reduce SO_4^{2-} diffusion stemming from their inherent ordered channels, [29] which is beneficial to guaranteeing stable Zn^{2+} flux and homogenizing Zn^{2+} distribution.

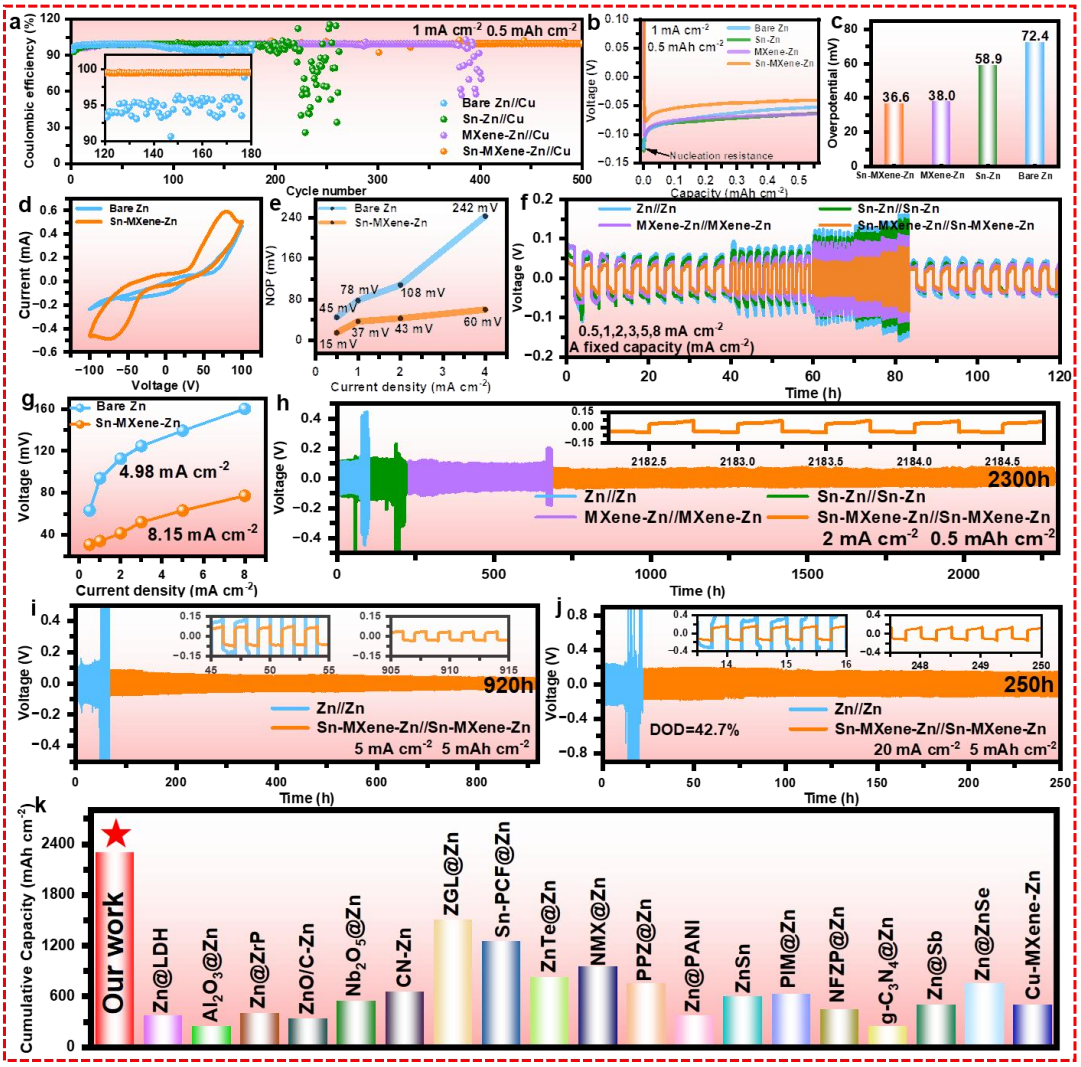

Figure 3. The electrochemical performance of symmetric and asymmetric cells. (a) CE profiles of the asymmetrical cells assembled by different electrodes at 1 mA cm^{-2}/0.5 mAh cm^{-2}. (b) Voltage–capacity curves for Zn deposition at 1 mA cm^{-2} on four different electrodes. (c) The summary of Zn nucleation overpotentials for four different electrodes. (d) CV curves of symmetric cells using bare Zn and Sn-MXene-Zn at a scan rate of 1.0 mV s^{-1}. (e) NOPs of Zn deposition on bare Zn and Sn-MXene-Zn at different current densities. (f) Rate performance of symmetric cells at current densities from 0.5 to 8 mA cm^{-2} with a fixed capacity of 1 mAh cm^{-2} and (g) corresponding exchange current densities of bare Zn and Sn-MXene-Zn. Long-term galvanostatic cycling performance of symmetric cells at current densities/capacities of (h) 2 mA cm^{-2}/0.5 mAh cm^{-2}, (i) 5 mA cm^{-2}/5 mAh cm^{-2} and (j) 20 mA cm^{-2}/5 mAh cm^{-2}. (k) Comparison of the Sn-MXene-Zn electrode with recently reported Zn anodes using artificial interfacial layer strategy.

The directional growth of zinc deposits, inhibited side reactions and rapid ion transport obtained by multifunctional Sn-MXene layer are expected to strongly boost the electrochemical performance of zinc anodes. Firstly, CE (the ratio of stripping

capacity to plating capacity per cycle) measurements are performed by Zn//Cu asymmetric cells to assess the plating/stripping reversibility of Zn under Sn-MXene protection. As revealed in Figure 3a, the cells including the bare Zn//Cu, Sn-Zn//Cu and MXene-Zn//Cu show an unstable state for CE and short cycle life as a result of localized short-circuiting. The result indicates that no significant effect of the Sn coating and MXene coating on inhibiting zinc dendrite propagation and corrosion. In striking contrast, the much better reversibility and stability are identified for the optimized Sn-MXene-Zn//Cu cell with an ultrahigh average CE of ≈ 99.3% for over 500 cycles (500 h) at a current density of 1 mA cm^{-2} with a capacity of 0.5 mAh cm^{-2}, enabling ≈ 4-fold elongation of the longevity compared with bare Zn. As depicted in the corresponding plating/stripping voltage curves using Zn//Cu cells in different cycles (Figure S16, Supporting Information), stable voltage curves with negligible variation are acquired in the Sn-MXene-Zn//Cu cell, in which a considerably lower polarization potential is observed at ≈ 70 mV after the activation process in contrast to that of the cell with bare Zn//Cu (≈150 mV). The exceptional CE and low polarization potential confirm improved ionic transfer kinetics in the interface between Sn-MXene and the electrolyte. The relatively smaller initial nucleation overpotential of 36.6 mV is obtained as Zn plating on the Sn-MXene layer, which is smaller than those of on the MXere layer (38.0 mV), Sn layer (58.9 mV) and bare Zn (72.4 mV), which might be due to the nucleation effect and accessible active sites on Sn-MXene (Figure 3b-c). Similar phenomenon can also be observed at higher current density of 5 mA cm^{-2}, and the asymmetric cell with modified Sn-MXene still achieves best cycling stability with a highest average CE during extended cycle life compared with asymmetric cells based on bare Zn, Sn-Zn and MXene-Zn, even after 500 cycles (Figure S17, Supporting Information). The permanent failure of the asymmetric battery without modified is easily observed after cycling for ≈ 70 cycles, accompanied by abrupt CE value drops and rises in severely fluctuating profiles. The nucleation overpotential on Sn-MXene-Zn is maintained at ≈ 42.3 mV, still much lower than that of undecorated Zn anode (≈122.3 mV) (Figure S18, Supporting Information), also confirming

favorable durability and superior reversibility for the multi-interface regulation effect. The facilitated reversibility and electrochemical kinetics are further certified by the cyclic voltammetry (CV) measurement at a scan rate of 0.1 mV s^{-1} (Figure S19, Supporting Information). The highest intense peak current of the Sn-MXene-Zn reflects the fastest reaction kinetics resulting from the abundant zincophilic nucleation sites.[30] Also, in the XPS spectrum of the cycled Sn-MXene-Zn anode (Figure S20, Supporting Information), the atomic ratio of Zn to Cl reaches 7.4, indicative of the coverage of Zn on the electrode surface.

To well clarify the acceleration of ion transport using Sn-MXene layer, the EIS of symmetric cells are conducted (Figure S21, Supporting Information). Apparently, The Sn-MXene-Zn symmetric cell displays the smallest charge transfer resistance (R_{ct}) among four anodes, suggesting the fastest charge transfer and Zn dissolution/deposition kinetics induced by the Sn-MXene interfacial layer. Detailed electrochemical investigations are further performed to study reversibility and electrochemical kinetics of bare Zn and Sn-MXene-Zn during the plating/stripping process, CV measurements of symmetric cells are implemented at a scan rate of 1 mV s^{-2} (Figure 3d and Figure S22, Supporting Information). Sn-MXene-Zn harvests a larger area of integration peak and higher maximal current density in comparison with un-modified Zn, suggesting that improved kinetic and interfacial activity to Zn deposition. Moreover, the CV curves of Sn-MXene-Zn retains identical shapes from the 1st to 3rd cycles compared to the gradually changing peaks of the original Zn, again manifesting the superior reversibility of the Zn plating/stripping process in the Sn-MXene-Zn cell. Considering that initial Zn nucleation is critical to elucidating the transition process of Zn dendrites, the notable comparison of potential difference (NOP) values for symmetric cells at diverse current densities (Figure S23, Supporting Information) indicates the role of Sn-MXene-Zn in Zn deposition kinetics. During initial deposition at a current density of 0.5 mA cm^{-2}, Sn-MXene-Zn shows a low NOP of only 15 mV, much smaller than that of bare Zn (45 mV), which reflects that Sn-MXene layer can effectively reduce the Zn nucleation barrier and strongly enhance

Zn^{2+} transport and diffusion. Similarly, as shown in Figure 3e, more defined differences in NOPs are quantified even at higher current densities (1, 2, and 4 mA cm^{-2}), which favor uniform zinc nucleation and smooth zinc deposition behavior in rapid Zn plating processes enabled by the superior ionic conductivity and Zn^{2+} sieving (ion-selective) characteristics of Sn-MXene-Zn, thus endow the cells with considerably good electrochemical performance. A rate performance for symmetric cells is compared at a capacity of 1 mAh cm^{-2} (Figure 3f and Figure S24, Supporting Information), where the Sn-MXene-Zn cell always presents lower hysteresis and more stable voltage plateau at various current densities. When the current increases to 8 mA cm^{-2}, the polarization of bare Zn soars to 160.9 mV originating from sluggish ion transfer, whilst merely 77.2 mV is achieved for Sn-MXene-Zn. To accurately assess the zinc deposition kinetics based on rate performance testing (Figure 3g), the exchange current density (i_0), which is closely related to the Zn electrodeposition process, is calculated by the Butler-Volmer approximation equation (Equation S3, Supporting Information).[25b] According to the linear fitting, a higher i_0 of 8.15 mA cm^{-2} is obtained for Sn-MXene-Zn in contrast to i_0 of 4.98 mA cm^{-2} for bare Zn, directly demonstrating the decreased the overpotential and facilitated Zn deposition kinetics by the multi-interface regulation.

Subsequently, a long-term zinc plating/striping cyclic measurement is performed using typical Zn//Zn symmetric cells under different current densities. As expected, the symmetric cell with Sn-MXene-Zn presents a more stable voltage hysteresis of around 62.5 mV and an extended lifespan for ≈ 2300 h at 2 mA cm^{-2} with a fixed capacity of 0.5 mAh cm^{-2} (Figure 3h). In stark contrast, the symmetric batteries of bare Zn, Sn-Zn and MXene-Zn show higher voltage hysteresis and lost the voltage characteristic curve after 71, 178 and 660 h, respectively. Notably, the corresponding apparent volume expansion of the bare cell and intense dendrite extension in separator after cycling, while it is suppressed without bulging in the symmetrical cell fabricated using the Sn-MXene anode, suggesting suppressed hydrogen evolution and menacing dendrites are well demonstrated in the symmetric cell using Sn-MXene (Figure S25,

Supporting Information). Such perfect enhancement of cyclic reversibility and stability suggests that the Sn-MXene coating is exceptionally effective in stabilizing zinc electrodeposition. An increase in current density will cause an uneven electric field at the anode/electrolyte interface, resulting in unfavorable nucleation.[31] In order to further demonstrate the advanced effect of Sn-MXene interface layer on anode stabilization, the cyclic tests with higher current density/capacity are implemented. At a higher current density of 5 mA cm^{-2} with a plating/stripping capacity of 5 mA cm^{-2}, impressively, the cell with bare Zn is vulnerable to show a stronger voltage hysteresis, along with a large amplitude of voltage fluctuation after only ≈ 50 h caused by aggravated growth of dendritic Zn resulting from the apparently non-uniform current/ion distribution. For Sn-MXene-Zn, however, it delivers a ≈ 18-fold improvement in cycle life (920 h) without notable fluctuations that of bare Zn (Figure 3i). Considering that the high depth of discharge (DOD > 40%) is crucial for practical applications, the zinc plating/stripping cycling is further evaluated under a harsh condition with the current density/capacity of 20 mA cm^{-2}/5 mA cm^{-2} (the thickness of the zinc foil is 20 μm, corresponding to a DOD of ≈ 42.7%). More surprisingly, the Sn-MXene-Zn anode could maintain highly stable cycling for 250 h with the relatively lower overpotentials and the smoother plating/stripping processes, while the symmetrical battery assembled by the bare Zn suffers from violent voltage fluctuations and polarization with a poor cycling life of merely ≈ 13 h, arising from dendrite-induced short-circuit and corrosion (Figure 3j). This stable Zn deposition behavior of Sn-MXene-Zn at 8 mA cm^{-2} is also demonstrated by ex-situ SEM, XRD and XPS images after 45 h (Figure S26-30, Supporting Information). Many hexagonal by-products, "dead zinc" deposits and dendrites in bulk are observed at bare Zn in the SEM, which are potentially dangerous and give rise in intracellular short circuits. In contrast, the surface of the Sn-MXene-Zn electrode still maintains a highly dense and compact structure, with almost no by-products or dendrites after cycling, which are consistent with XRD and XPS results. Also, the S element in the EDS mapping of post-cycling Sn-MXene-Zn is almost non-existent. On the contrary, the presence of S

in post-cycling bare Zn can be attributed to the production of by-products. The same results can be acquired at current densities/capacities of 5 mA cm^{-2}/1.25 mAh cm^{-2}, 1 mA cm^{-2}/0.25 mAh cm^{-2} and 0.5 mA cm^{-2}/0.125 mAh cm^{-2} (Figure S31, Supporting Information). Compared with previously reported APL@Zn electrodes, the cycling time (920 h) and cumulative capacity (2300 mAh cm^{-2}) in our work are particularly competitive in terms of regulating the stability of zinc electrodeposition due to the multi-interface regulation effect of Sn and $Ti_3C_2Cl_2$ MXene (Figure 3k and Table S2, Supporting Information).

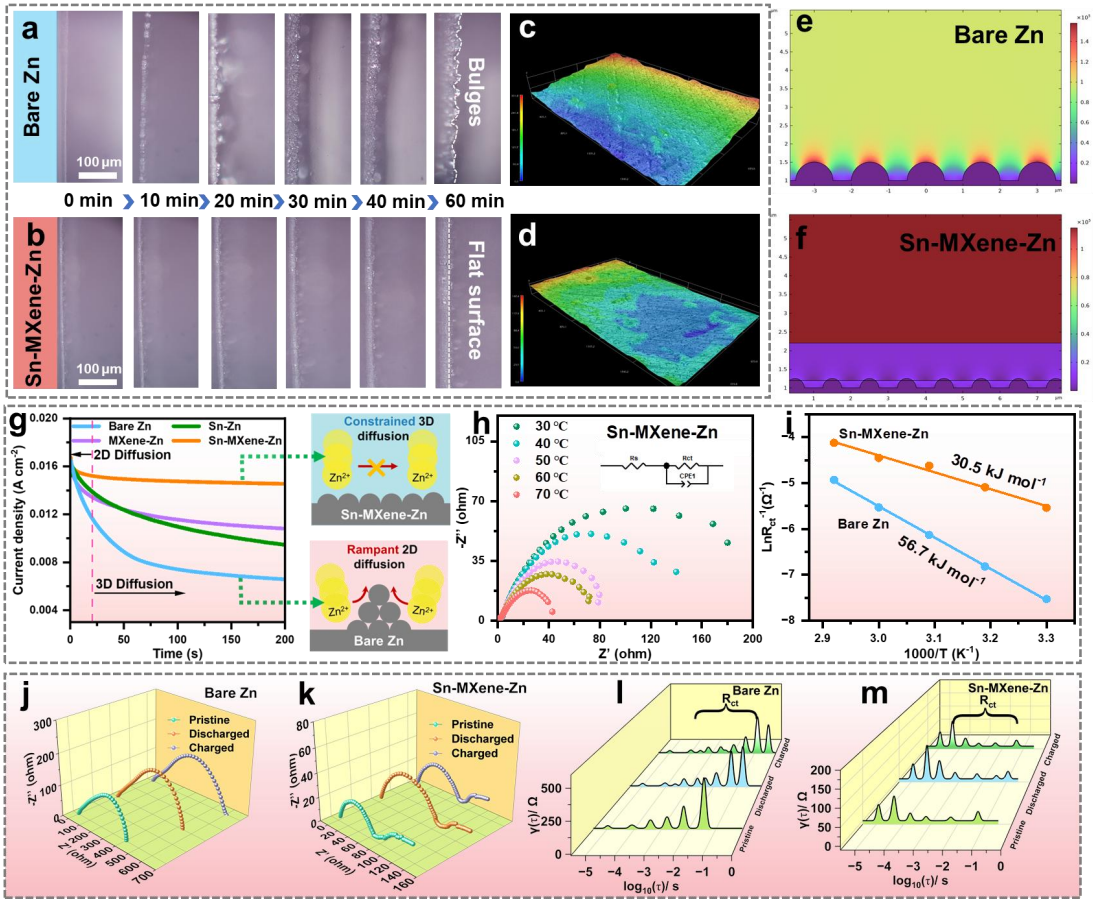

Figure 4. In situ optical microscope images of (a) bare Zn and (b) Sn-MXene-Zn anodes at 5 mA cm^{-2} and (c-d) the corresponding optical microscope images after 60 min. Simulated electric field distributions (e) on the bare Zn and (f) on the Sn-MXene-Zn electrodes. (g) CA tests of different electrodes at -150 mV overpotential. The EIS curves of (h) Sn-MXene-Zn symmetrical cell at different temperatures. Inset is the equivalent circuit. (i) The calculated desolvation activation energies of bare Zn and Sn-MXene-Zn electrodes. EIS curves of (j) bare Zn and (k) Sn-MXene-Zn cells during EIS measurements, and corresponding analysis of distribution of DRT upon galvanostatic in (l) bare Zn and (m) Sn-MXene-Zn, respectively.

To visually monitor the dynamic Zn deposition state, the in-situ optical microscopy equipped with a homemade transparent Zn//Zn symmetric cell was employed at the relatively large current density of 5 mA cm^{-2} for 60 min (Figure S32, Supporting Information). As shown in Figure 4a, the obvious randomly distributed Zn protrusions begin to emerge on the surface of exposed Zn foil after 20 min electrodeposition. With prolonged electrodeposition, the numerous mossy-like zinc dendrites are found, displaying an extremely rough surface on account of the notorious ‘‘tip effect’’. Comparatively, a relatively uniform and smooth Zn deposition on the Sn-MXene-Zn surface is maintained throughout the Zn plating process with no sign of striking Zn protrusion and zinc dendrite formation, except for a slight increase in thickness (Figure 4b). The large height difference in plating uniformity is also highlighted by the 3D optical surface-profilometry images. Bare Zn metal shows a significant non-uniform distribution and rugged surface with some protrusions after plating 60 min because of the vertical dendrite growth (Figure 4c), while Sn-MXene-Zn anode is conspicuously more uniform with minimum altitude intercept in plating thickness (Figure 4d). which is also evidence of the homogeneous zinc deposition. The electric field distribution on the bare Zn and Sn-MXene-Zn electrodes is further monitored by adopting the numerical simulation. For the bare zinc anode, inhomogeneous surface electric filed distribution results in nonuniform zinc deposition. Once the irregular protuberances appear, the electric field intensity will be strengthened around the tips, and eventually forming tip hot spots and bulky dendrites (Figure 4e). Meanwhile, the Sn-MXene-Zn interfacial layer with electronic shielding effect renders the charges and Zn-ion flux redistributed and homogenized, strongly reducing irregular zinc gathering near these protrusions, which thereby guarantees planar and dendrite-free zinc deposition (Figure 4f).

The CA tests of the electrodes with and without coatings is also monitored to further gain a deeper insight into the early Zn deposition behaviors. At an overpotential of –150 mV, it is found that the current density of electrodes with bare Zn, Sn-Zn and MXene-Zn display a continuous increase throughout the 200 s,

corresponding to the long-time and frantic 2D diffusion process of Zn^{2+}, which leads to the uneven deposition and the eventual propagation of dendrites by lateral diffusion. Due to the "tip effect", the adsorbed Zn^{2+} tends to laterally diffuse two-dimensionally to sites associated with minimum specific surface energy or the exposed area.[32] Unlike that, the time for the current density of the Sn-MXene-coated Zn electrode with to be equilibrium significantly shortens to around 20 s, evidencing the achievement of stable 3D diffusion after the quickly finished 2D diffusion of Zn^{2+}. The rapid arrival for 3D Zn^{2+} diffusion proves that the regulated and stable out-of-plane diffusion for adsorbed Zn^{2+} on the Sn-MXene surface with zincophilic feature is obtained by passing through the Sn-MXene layer. It has been verified that de-solvation of Zn ion is the critical obstacle for charge migration on the Zn deposition chemistry. In addition to the above advantages, the Sn-MXene-Zn interphase is also expected to be beneficial to the de-solvation of hydrated Zn^{2+} ($[Zn(H_2O)_6]^{2+}$).Hence, the Arrhenius activation energy (E_a) can be quantitatively estimated based on the Arrhenius formula (Equation S4, Supporting Information).[16a, 33] To determine effect of the de-solvation, the R_{ct} of the symmetric cells including bare Zn and Sn-MXene-Zn is acquired via EIS profiles at various temperatures from 30 to 70 °C (Figure 4h and Figure S33, Supporting Information). Obviously, the R_{ct} obtained of the Sn-MXene-Zn is several times smaller than that of bare Zn at each temperature, resulting in evidence that enhanced charge transfer kinetics in the Sn-MXene-Zn cell. According to the experimental results by linear fitting, the E_a of the Sn-MXene-Zn cell is calculated to be only 30.5 kJ mol^{-1}, which is about half of the counterpart (56.7 kJ mol^{-1}) (Figure 4i), revealing that Sn-MXene-Zn could strongly promote Zn^{2+} de-solvation and ionic transfer kinetics in the process of Zn plating enabled by the reducing energy consumption, weakening the coordination of H_2O molecules in solvated sheath of Zn^{2+}. For more in-depth research on the interfacial kinetics, the in-situ EIS spectra of bare Zn and Sn-MXene Zn cells are recorded (Figure 4j-k) and the corresponding EIS curves are analyzed by through the distribution of relaxation times (DRT) (Figure 4l-m). [34] The peaks with relaxation time $\log_{10}(\tau)$ of ~-4 s − ~-1 s are

ascribed to the charge transfer process of Zn^{2+} ions cross the interface (R_{ct}). It can be clearly seen that the interfacial charge transfer impedance in the bare Zn increases significantly after plating/stripping, while the cell containing Sn-MXene-Zn remains relatively constant, indicating intrinsically faster kinetics and corresponding to a significant decrease of the byproducts.

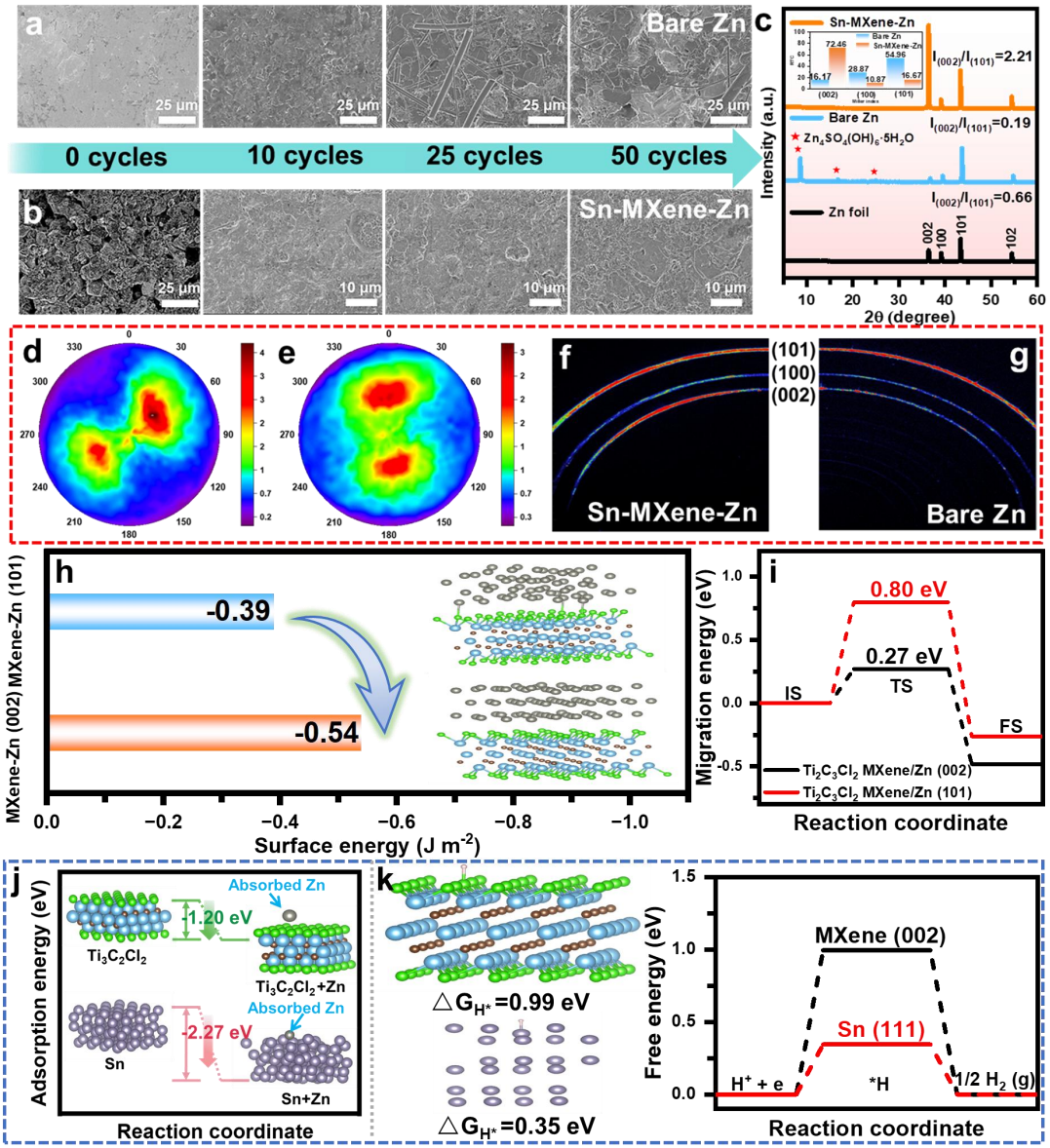

Figure 5. The SEM of (a) bare Zn and (b) Sn-MXene-Zn anodes after different cycles at 1 mA cm^{-2} with capacity of 1 mAh cm^{-2}. (c) The corresponding XRD analysis of the bare Zn and Sn-MXene-Zn anodes after 50 cycles. The (002) pole figures of the Zn deposits in (d) Sn-MXene-Zn and (e) bare Zn at 5 mA cm^{-2} with a capacity of 1 mAh cm^{-2}. The 2D GIWAXS results of Zn anodes after 50 cycles in (f) Sn-MXene-Zn and (g) bare Zn at 5 mA cm^{-2} with a capacity of 1 mA

h cm^{-2}. (h) The comparison of the Sn-MXene-Zn (101) and Sn-MXene-Zn (002) calculated surface energy. (i) The energy barriers of Zn^{2+} diffusion at these interfaces. (j) The binding energies of Sn and $Ti_3C_2Cl_2$ MXene to Zn atoms. (k) The free-energy diagram on the Sn (111) and $Ti_3C_2Cl_2$ MXene (002) surfaces for the HER.

In addition to the ability of ion migration manipulation, the regulation of zinc electrodeposition morphology is another significant factor affecting the inhibition of zinc dendrites and corrosion during repeated cycling. The morphology evolution of both bare Zn and Sn-MXene-Zn electrodes after 0, 10, 25, and 50 electroplating/stripping cycles at a current density of 1 mA cm^{-2} with a cutoff capacity of 1 mAh cm^{-2} is characterized by ex-situ SEM technology. After cycling for only 10 cycles, the random accumulation of moss-like zinc deposits adhering to glass fibers (from the separator) and massive "dead zinc" products are generated on the post-cycling bare Zn due to rampant growth of zinc dendrites and severe electrolyte corrosion (Figure 5a), which are to lead high current density at the tip sites, disrupt the homogenization of Zn^{2+} diffusion, and ultimately aggravate dendrites growth in subsequent cycles. As illustrated by SEM images (Figure S34, Supporting Information), the surface of Sn-Zn and MXene-Zn anodes remained smooth and compact without dendrites during the initial platting/stripping process, but after 25 cycles the hexagonal dendrites can be clearly observed. Interestingly, for Sn-MXene-Zn system, after cycling for even 50 cycles, the surface morphology of a compact and dendrite-free deposition with no visible structural change is kept, which favors the more homogeneous and orderly Zn^{2+} transport channels in Sn-MXene (Figure 5b). which is consistent with the cross-sectional SEM images after cycling for 50 cycles (Figure S35, Supporting Information). This suggests the manipulation of Zn electrodeposition by the Sn/MXene layer is inferior to the Sn-MXene composites. It is also found that after 50 cycles, the increase in thickness of the symmetrical Zn cell in Sn-MXene-Zn (1.01%) is much smaller than that of the cell in bare Zn (7.84%) (Figure S36, Supporting Information). The orientation of deposited zinc on fresh Zn, cyclic bare Zn and Sn-MXene-Zn electrodes has been revealed by XRD result. Specifically, the intensity ratio (R= I_{002}/I_{101}) of Zn (002) and Zn (101) is employed to

estimate the orientation of the Zn platelet deposition.[31] As shown in Figure 5c, comparing with fresh Zn and Sn-MXene-Zn anode, the *R* value of $I_{(002)}/I_{(101)}$ dramatically increases from 0.66 for Zn anode without cycling to 2.21 for Sn-MXene-Zn anode after 50 cycles, revealing the dominant role of preferential orientation of Zn electrodeposition along (002) modulated by multi-interface regulation. This might originate from the fact that the Zn platelets by modified prefers horizontal and continuous growth. The RTCs of typical zinc crystal planes ((002), (100), and (101)) of the plated Zn electrodes are calculated from the following formula: $RTC_{(hkl)} = \frac{I_{(hkl)}/I_{0(hkl)}}{\sum(I_{(hkl)}/I_{0(hkl)})} \times 100$ (Equation 3).[1e] The higher the RTC value, the more prominent the texture.[1e] As depicted in the inset of Figure 5c, an increased RTC of (002) plane from 16.17 to 72.46 is observed when added Sn-MXene along with the decline of (100) and (101) RTC. This result further reveals that highly exposed (002) crystal plane cultivated by the Sn-MXene layer. Furthermore, the diffraction peaks of byproducts ($Zn_4SO_4(OH)_6 \cdot 5H_2O$) are almost invisible in the XRD patterns of the cycled Sn-MXene-Zn anode in contrast to the bare Zn, certifying the preeminent anti-passivation effect of Sn-MXene-Zn anode. Additionally, the structural and texture information of deposited Zn are ulteriorly investigated adopting X-ray diffraction pole patterns and 2D GIWAXS figures. As displayed in Figure 5d-e, the pole intensity of the (002) basal plane for bare Zn is 3, whilst optimized Sn-MXene-Zn exhibits an enhanced intensity of 4, verifying that the texture structure along the (002) direction for the Zn platelets, a thermodynamic preferred Zn (002) crystal plane growth with the lowest surface energy (Figure 5d).[35] Meanwhile, an arbitrary growth of Zn^{2+} on the unmodified Zn surface will cause a wide range of grain orientations. This causes the (002) pole figure to display a broad pattern of the diffraction intensity, revealing that its less textured orientation along (002) (Figure 5e). Regarding Sn-MXene-Zn anode, the 2D GIWAXS patterns of Zn deposition illustrate that the (002) crystal plane possesses the more dominant and conspicuous diffraction intensity. Moreover, a distinct intensity fluctuation can be recognized along the (002) Debye ring (Figure 5f). This observation demonstrates the preferential orientation of the Zn (002) crystal plane

again, in contrast to the inconspicuous (002) and (100) planes in the bare Zn (Figure 5g). This reflects that the Zn deposits in bare Zn anode possesses a polycrystalline feature with a disordered orientation, while in the Sn-MXene-Zn system, the size of Zn grain is relatively larger and the orientation is more evident. Considering the above results, it is reasonable to conclude that the crucial role of highly oriented Zn (002) deposition manipulated by multifunctional interface in ameliorating the stability and reversibility of the Zn anode.

Considering the different crystal textures of Sn-MXene-Zn (101) and Sn-MXene-Zn (002) electrodes, the effect of structure-related surface energy on zinc deposition is further studied by first-principles calculations. In theory, the Zn (002) plane possesses the lowest surface energy, compared to other lattice planes as a result of the intrinsic hcp structures. Figure 5h depicts that the $Ti_3C_2Cl_2$ MXene-Zn (002) has a lower surface energy (–0.54 J m^{-2}) than that of the $Ti_3C_2Cl_2$ MXene-Zn (101) (–0.39 J m^{-2}). A significant reduction in the surface energy of Zn (002) implies a reduction in the nucleation resistance of Zn (002). As previously analyzed, $Ti_3C_2Cl_2$ MXene can significantly improve migration kinetics of Zn^{2+}, combined with further decreased Zn (002) surface energy, thereby Zn deposition with (002) preferential orientations become available. The interaction between adsorbed Zn^{2+} and APL plays a crucial role in manipulating the distribution of Zn nucleation to induce homogeneous Zn deposition. Indeed, the Zn^{2+} diffusion is strongly hindered by hard de-solvation of hydrated Zn^{2+}, heterogeneous Zn^{2+} flux distribution, and the high concentration polarization. Here, the diffusion energy barriers of Zn^{2+} along the interface of Sn-MXene-Zn (101) and Sn-MXene-Zn (002) are compared in Figure 5i. The diffusion energy barrier of Zn^{2+} at the interface of Sn-MXene-Zn (002) is 0.27 eV, which is much smaller than that of Sn-MXene-Zn (101) (≈ 0.80 eV). A low diffusion energy barrier of the (002) plane is beneficial for the fast transport of Zn^{2+} and the uniform distribution of Zn^{2+}, especially at high rates. In order to better elucidate how the APL prepared by Sn-MXene can change the adsorption behavior of Sn-MXene-Zn on Zn^{2+}, the binding energy of Zn ion is investigated adopting density functional

theory (DFT) calculations. The binding energies of Zn ion on Sn-Zn (–2.27 eV) and $Ti_3C_2Cl_2$ MXene (–1.20 eV) are more negative than that on bare Zn (–0.16 eV) (Figure 5j),[36] suggesting that a lower energy barrier and higher selectivity of adsorption for Zn on the Sn-MXene surface compared with metallic Zn, which strengthen the capability capture and transfer of Zn^{2+} at the Sn-MXene interface in the plating/stripping process. The high Zn affinity of Sn-MXene can also boost homogenous Zn^{2+} flux through interface of the anode-electrolyte and eliminate of the hydration sheath in $[Zn(H_2O)_6]^{2+}$, thereby improving the dendrite-free deposition behavior of Sn-MXene-Zn during cycling.[25b] It has been reported that the free energy of hydrogen adsorption on Zn (101) is close to the thermoneutral state (≈ 0.18 eV),[3b] meaning that the easy occurrence of hydrogen evolution. The free energy of hydrogen adsorption (0.99 eV) on $Ti_3C_2Cl_2$ MXene (002) is quite above 0 eV (Figure 5k), implying that enormous difficulty for hydrogen evolution from its surface. Although compared with Zn (101), the free energy of hydrogen adsorption on metallic Sn (200) is higher. Nevertheless, compared with $Ti_3C_2Cl_2$ MXene, metallic Sn possesses a relatively weaker ability to could suppress the HER.

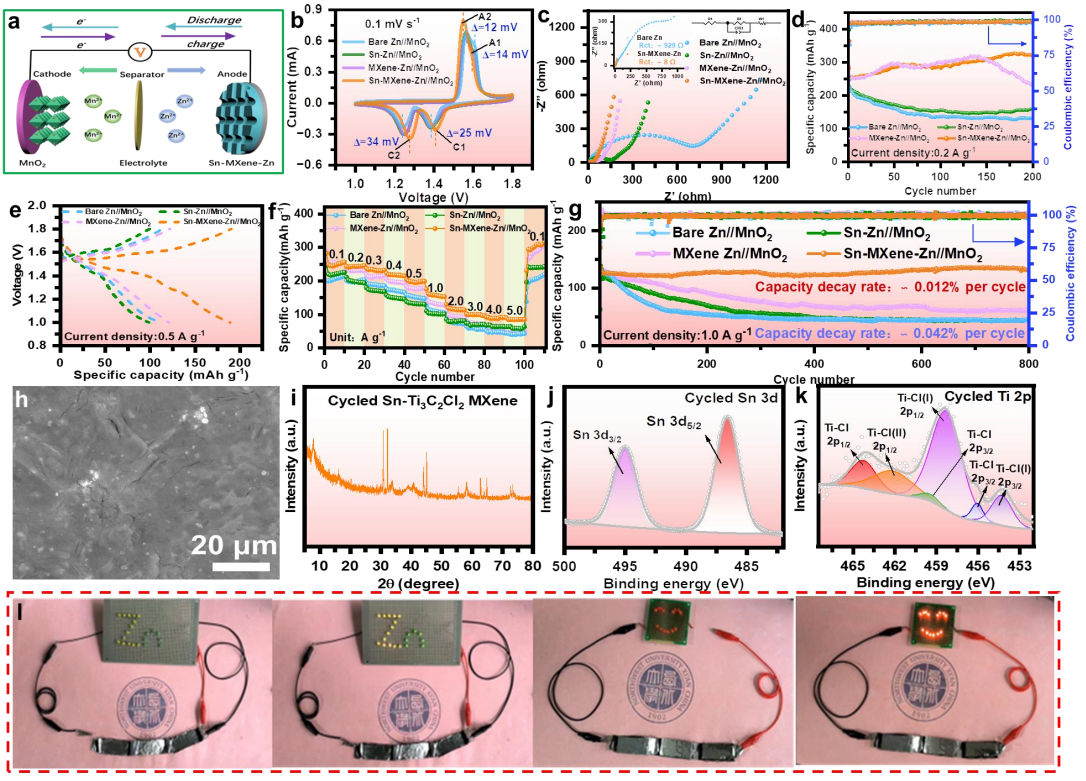

Figure 6. The electrochemical performance investigation of aqueous Zn//MnO_2 batteries. (a) Schematic of the Zn-ion battery device. (b) CV curves at 0.1 mV s^{-1}, (c) EIS plots, (d) cycling stability at 0.2 A g^{-1}, (e) GCD profiles at 0.5 A g^{-1} (600^{th} cycle), (f) Rate performance and (g) Long-term cycling performance at 1 A g^{-1} of different full cells. (h) SEM image, (i) XRD pattern and XPS spectra of (j) Sn 3d and (k) Ti 2p for Sn-MXene after 100 cycles at 1 A g^{-1}. (l) A picture of three-connected cells lighting up an LED light.

Inspired by the successful construction of multi-interface regulation, the practicability of the Sn-MXene-Zn anode was tested systematically by Zn-ion full batteries employing α-MnO_2 and $NH_4V_4O_{10}$ as cathodes (Figure S37, Supporting Information).[1e, 37] The zinc-metal full battery (Zn//MnO_2) is constructed, as schematically illustrated in Figure 6a. Here, $MnSO_4$ (0.1 M) is added to the electrolyte (2 M $ZnSO_4$) to suppress the disproportionation reaction of MnO_2 cathode. The two pairs of well-defined redox peaks for the Zn//MnO_2, Sn-Zn//MnO_2, MXene-Zn//MnO_2 and Sn-MXene-Zn//MnO_2 cells corresponding to H^+ and Zn^{2+} insertion/extraction into/from α-MnO_2 are observed in the CV curves in the voltage range of 1–1.8 V (Figure 6b and Figure S38-39, Supporting Information).[38] Noticeably, the full cell using the Sn-MXene-Zn anode harvests higher reduction voltages but lower oxidation voltages than those of other cells, indicative of ameliorated reaction kinetics. Meanwhile, after the first cycle, the following CV curves display similar shapes, revealing a reversible electrochemical process. Moreover, the similar CV shapes of the four devices indicates that a negligible effect of the coating interface on the original electrochemistry in Zn//MnO_2 full batteries. According to the relationship between applied current (i) and scan rate (v): $i(V) = av^b$ (Equation 4), where a and b are adjustable constants, and i and v are applied current and scan rate. When the b value is around 0.5, the electrochemical reactions process is controlled by diffusion mechanism, while the b value of 1.0 suggests that the surface-controlled response is leading.[39] Here, the calculated b values of peaks 1, 2, 3, and 4 for the cells with Sn-MXene-Zn are 0.52, 0.58, 0.70, and 0.51, respectively, which are larger than that of the cell with bare Zn (Figure S40, Supporting Information), indicating that the Sn-MXene layer facilitates the surface-controlled process. Additionally, the Zn^{2+}

diffusion coefficients (D_{Zn}^{2+}) are calculated based on the Randles-Sevcik equation (Equation S5, Supporting Information) adopting the CV tests of the Zn//MnO_2 cells.[40] The D_{Zn}^{2+} of the Sn-MXene-Zn//MnO_2 cell is larger than that of the bare Zn//MnO_2 cell in all cathodic and anodic reactions (Figure S41, Supporting Information), which gives rise in a redistribution of the Zn^{2+} flux and a faster transport of Zn^{2+}. As illustrated by the equivalent circuit and Nyquist plots (Figure 6c), the optimized Sn-MXene-Zn//MnO_2 cell exhibits the smaller charge transfer resistance than that of the device assembled with other anodes, which is in accordance with its smaller polarization. After cycling, the Sn-MXene-Zn//MnO_2 cell still displays smaller R_{ct} than that of bare Zn//MnO_2 cell. The effectiveness of the Sn-MXene protective layer on the Zn surface is further elevated through cycling performance. The cell operated in Sn-MXene-Zn//MnO_2 can consistently undergo a capacity increase and improve initial capacities from 255.3 mAh g^{-1} to 321.6 mAh g^{-1} during 200 cycles at a low current density of 0.2 A g^{-1} with a stable CE of ≈ 100% (Figure 6d). The capacity increase with the increase of cycles is mainly attributed to the deposition of Mn^{2+} onto the surface of the cathode to form MnO_x, especially at a low current density.[41] However, bare Zn based full cell is sharply decreased from the initial capacity of 245.8 mAh g^{-1} to 131.8 mAh g^{-1}. Similarly, the current density goes up to 0.5 A g^{-1}, a stable reversible capacity of 189.7 mAh g^{-1} can be realized by Sn-MXene-Zn//MnO_2 battery after 600 cycles, which is about twice the capacity maintained with Zn//MnO_2 tested under the same conditions (Figure 6e and Figure S42, Supporting Information). Profiting from the significant superiorities of the Sn-MXene-Zn anode, the rate performance at the stepwise increased current densities from 0.1 to 5.0 A g^{-1} in Sn-MXene-Zn//MnO_2 cell and the corresponding charge-discharge curve is investigated (Figure 6f and Figure S43, Supporting Information), where its capacities are consistently the highest among the four cells. Even at a high current density of 5.0 A g^{-1}, the specific capacity of the Sn-MXene-Zn//MnO_2 cell is maintained at 89.2 mAh g^{-1}, whereas the reversible capacity is extremely low (≈ 40.2 mAh g^{-1}) for the bare Zn//MnO_2 cell. Meanwhile, the higher-rate cycling mode of 1.0

A g^{-1} is adopted so as to further verify the superiority of Sn-MXene-Zn//MnO_2 cell. The impressive discharge capacity of 131.4 mAh g^{-1} at 1.0 A g^{-1} can be maintained in Sn-MXene-Zn//MnO_2 cell after 800 cycles, corresponding to a slow capacity loss rate of ≈ 0.012% per cycle and a stable CE of nearly 100% (Figure 6g), superior to those of the cells with bare Zn, Sn-Zn and MXene-Zn, with reversible capacities of 43.9 (capacity decay rate: ≈ 0.042% per cycle), 44.6 and 60.5 mAh g^{-1} after 800 cycles at 1.0 A g^{-1}. It is worth mentioning that the facilitated cycling stability of Sn-MXene-Zn//MnO_2 full cells outperforms most of the reported modified Zn electrodes (Table S3, Supporting Information), suggesting good potential for providing stable zinc deposition kinetics to ameliorate the electrochemical performance of commercial AZIBs. From the morphologies, significant amounts of insulating byproducts and Zn dendrites are identified on post-cycling surface of bare Zn, whereas the surface of the zinc anode with Sn-MXene coating remains relatively flat and smooth after 100 cycles at 1.0 A g^{-1} (Figure 6h and Figure S44-46, Supporting Information), which is proved to be favorable evidence for boosting the reversibility of Zn deposition. The XRD tests (Figure S47, Supporting Information) and ex situ 3D optical microscope images (Figure S48, Supporting Information) also confirm the benefits for the cell with Sn-MXene-Zn//MnO_2. It should be noted that the $I_{(002)}/I_{(101)}$ of Sn-MXene anode increases to 2.16 after cycling, fully verifying the Zn (002) oriented electrodeposition regulated by the Sn-MXene layer. What's more, the peaks of the XRD pattern show that the crystallinity of Sn-MXene is still wonderful after 100 cycles (Figure 6i), which is also confirmed by XPS spectra (Figure 6j-k and Figure S49, Supporting Information). Lastly, the advantage of Sn-MXene-Zn in suppressing the self-discharge phenomenon is explored by measuring the open-circuit voltage (OCV) attenuation of a fully charged Zn//MnO_2 battery for 24 h of resting and the specific capacities during the process of subsequent discharging to 1.0 V at 1 A g^{-1}. As shown in Figure S50, Supporting Information, 1.53 V of OCV during 24 h resting and high CE of 95.4% are delivered in the cell with Sn-MXene-Zn anode, surpassing the 90.9% and 1.47 V for the cell with bare Zn//MnO_2, which confirms that Sn-MXene layer effectively

facilitates anti-self-discharge behaviors and the structural stability of aqueous Zn metal battery. More meaningfully, this device can light up a LED indicator light, which again confirms the feasibility of the Sn-MXene-Zn//MnO_2 batteries for energy storage (Figure 6i). In addition to MnO_2 cathode, $NH_4V_4O_{10}$ cathode is employed to match with Sn-MXene-Zn or bare Zn anodes, constructing full cells. As shown in Figure S51, Supporting Information, CV curves of bare Zn//$NH_4V_4O_{10}$ and Sn-MXene-Zn//$NH_4V_4O_{10}$ cells at 0.1 mV s^{-1} within a voltage window of 0.35–1.4 V shows multi-step Zn storage mechanisms. The optimized Sn-MXene-Zn//$NH_4V_4O_{10}$ cell displays a much better cyclability that maintains a discharge capacity of 144.4 mAh g^{-1} after 4500 cycles at 10 A g^{-1}, while the bare Zn//$NH_4V_4O_{10}$ full cell shows dramatic capacity fading under the same cycling condition, showing the inferior irreversibility of Zn deposition. From these results, it is clear that a rationally designed multi-interface regulation contributes to the practical application of long-life zinc ion batteries for large-scale energy storage devices in the future.

3. Conclusion

In conclusion, the zincophilic and hydrophobic Sn-MXene composites is synthesized through a novel one-step molten salt etching process, and directly constructed on the Zn surface as a multifunctional interface for Zn anode. Experimental observations and DFT calculations indicate that zincophilic Sn with strong Zn binding ability can effectively lower the nucleation overpotential of Zn and homogenize Zn deposition, and this coating could promote the deposition of Zn with more exposed (002) plane, beneficial for the smooth and compact Zn plating. Meanwhile, the molten $SnCl_2$ etching endows the Sn-$Ti_3C_2Cl_2$ MXene with single -Cl termination, which enables the Sn-MXene to possess hydrophobic property, in favor of the de-solvation of the hydrated Zn^{2+} ions, and thus significantly mitigating the rampant HER and side reactions as well as the propagation of inert byproducts on the Zn electrode. Benefit from these advantages, the symmetric cell based on the Sn-MXene-Zn electrode displays a much-prolonged cycling life of over 920 h with a low voltage hysteresis (5 mA cm^{-2}, 5 mAh cm^{-2}). Even under the high depth of discharge

test (DOD ≈ 42.7%), Sn-MXene-coated Zn electrode exhibits a stable cycle performance for over 250 h, while the bare Zn fails after only 13 h. Moreover, the Sn-MXene-Zn//Cu cell reveals high and stable CE of above 99.3% for 500 cycles at 1 mA cm^{-2}, in sharp contrast to the bare Zn//Cu with a life of only 150 cycles and an average CE of 96.9%. Therefore, the assembled Sn-MXene-Zn//MnO_2 full cell delivers high stability during long-term 800 cycles at 1 A g^{-1}. The Sn-MXene coating with multi-interface regulation is highly efficient for stabilizing the Zn anode and it is expected to be a general strategy for other metal electrodes in aqueous batteries.

Acknowledgements

This work was supported by the National Natural Science Foundation of China (No. 22075227).

Conflict of interest

There is no conflict to declare.

References

[1] a) Y. An, B. Xu, Y. Tian, H. Shen, Q. Man, X. Liu, Y. Yang, M. Li, *Mater. Today* **2023**, *70*, 93; b) T. G. Yun, J. Lee, H. S. Kim, J. Y. Cheong, S. H. Kim, Y. Kim, S. Lee, I.-D. Kim, *Adv. Mater*. **2023**, 35, 2301141; c) X. Shi, Y. Sun, Y. Weng, X. Long, T. Lei, J. Zhou, D. Li, J. Zhang, Y. Huang, L. Ci, K. Li, T.-Y. Zhang, *Energy Environ. Sci*. **2023**, 16, 4670; d) X. Liu, F. Xu, Z. Li, Z. Liu, W. Yang, Y. Zhang, H. Fan, H. Y. Yang, *Coordin. Chem. Rev.* **2022**, 464, 214544; e) H. Zhang, Y. Zhong, J. Li, Y. Liao, J. Zeng, Y. Shen, L. Yuan, Z. Li, Y. Huang, *Adv. Energy Mater*. **2023**, 13, 2203254.

[2] a) L. Cao, D. Li, T. Pollard, T. Deng, B. Zhang, C. Yang, L. Chen, J. Vatamanu, E. Hu, M. J. Hourwitz, L. Ma, M. Ding, Q. Li, S. Hou, K. Gaskell, J. T. Fourkas, X.-Q. Yang, K. Xu, O. Borodin, C. Wang, *Nat. Nanotechnol*. **2021**, 16, 902; b) X. Liu, B. Xu, J. Lu, J. Han, S. Deng, X. Yu, Y. An, Y. Tang, *Small* **2023**, e2307557.

[3] a) S. Huang, R. Tang, X. Liu, Y. Zhang, Y. Tang, Z. Wen, M. Ye, Y. Yang, C. C. Li, *Energy Environ. Sci*. **2024**, 17, 591; b) P. Xiao, H. Li, J. Fu, C. Zeng, Y. Zhao, T. Zhai, H. Li, *Energy Environ. Sci*. **2022**, 15, 1638.

[4] a) L. Hong, L.-Y. Wang, Y. Wang, X. Wu, W. Huang, Y. Zhou, K.-X. Wang, J.-S. Chen, *Adv. Sci*. **2022**, 9, 2104866; b) K. Zhu, C. Guo, W. Gong, Q. Xiao, Y. Yao, K. Davey, Q. Wang, J. Mao, P. Xue, Z. Guo, *Energy Environ. Sci*. **2023**, 16, 3612.

[5] a) A. Chen, C. Zhao, J. Gao, Z. Guo, X. Lu, J. Zhang, Z. Liu, M. Wang, N. Liu, L. Fan, Y. Zhang, N. Zhang, *Energy Environ. Sci*. **2023**, 16, 275; b) Z. Zhao, R. Wang, C. Peng, W. Chen, T. Wu, B. Hu, W. Weng, Y. Yao, J. Zeng, Z. Chen, P. Liu, Y. Liu, G. Li, J. Guo, H. Lu, Z. Guo, *Nat. Commun*. **2021**, 12, 6606.

[6] Q. Ren, X. Tang, X. Zhao, Y. Wang, C. Li, S. Wang, Y. Yuan, *Nano Energy* **2023**, 109, 108306.

[7] Y. Zeng, P. X. Sun, Z. Pei, Q. Jin, X. Zhang, L. Yu, X. W. Lou, *Adv. Mater*. **2022**, 34, 2200342.

[8] P. X. Sun, Z. Cao, Y. X. Zeng, W. W. Xie, N. W. Li, D. Luan, S. Yang, L. Yu, X. W. Lou, *Angew. Chem., Int. Ed*. **2022**, 61, e202115649.

[9] T. Chen, Y. Wang, Y. Yang, F. Huang, M. Zhu, B. T. W. Ang, J. M. Xue, *Adv. Funct. Mater*.

2021, 31, 2101607.

[10] J.-L. Yang, P. Yang, W. Yan, J.-W. Zhao, H. J. Fan, *Energy Storage Mater*. **2022**, 51, 259.

[11] F. Ling, L. Wang, F. Liu, M. Ma, S. Zhang, X. Rui, Y. Shao, Y. Yang, S. He, H. Pan, X. Wu, Y. Yao, Y. Yu, *Adv. Mater*. **2023**, 35, 2208764.

[12] Q. Cao, Y. Gao, J. Pu, X. Zhao, Y. Wang, J. Chen, C. Guan, *Nat. Commun*. **2023**, 14, 641.

[13] J. Zheng, Q. Zhao, T. Tang, J. Yin, C. D. Quilty, G. D. Renderos, X. Liu, Y. Deng, L. Wang, D. C. Bock, C. Jaye, D. Zhang, E. S. Takeuchi, K. J. Takeuchi, A. C. Marschilok, L. A. Archer, *Science* **2019**, 366, 645.

[14] Y. Cheng, Y. Jiao, P. Wu, *Energy Environ. Sci*. **2023**, 16, 4561.

[15] J. Ruan, D. Ma, K. Ouyang, S. Shen, M. Yang, Y. Wang, J. Zhao, H. Mi, P. Zhang, *Nano-Micro Lett. 2023*, 15, 37.

[16] a) H. Liu, Z. Xin, B. Cao, Z. Xu, B. Xu, Q. Zhu, J.-L. Yang, B. Zhang, H. J. Fan, *Adv. Funct. Mater*. **2024**, 34, 2309840; b) X. Yang, W. Li, Z. Chen, M. Tian, J. Peng, J. Luo, Y. Su, Y. Zou, G. Weng, Y. Shao, S. Dou, J. Sun, *Angew. Chem., Int. Ed.* **2023**, 62, e202218454.

[17] a) X. Liu, M. Wang, B. Qin, Y. Zhang, Z. Liu, H. Fan, *Chem. Eng. J.* **2022**, 431, 133976; b) X. Liu, Z. Liu, W. Yang, M. Wang, B. Qin, Y. Zhang, Z. Liu, H. Fan, *Mater. Today Chem.* **2022**, 26, 101002; c) L. Liao, D. Jiang, K. Zheng, M. Zhang, J. Liu, *Adv. Funct. Mater*. **2021**, 31, 2103960.

[18] a) N. Zhang, S. Huang, Z. Yuan, J. Zhu, Z. Zhao, Z. Niu, *Angew. Chem., Int. Ed*. **2021**, 60, 2861; b) X. Zhu, X. Li, M. L. K. Essandoh, J. Tan, Z. Cao, X. Zhang, P. Dong, P. M. Ajayan, M. Ye, J. Shen, *Energy Storage Mater.* **2022**, 50, 243; c) H. Liu, Z. Xin, B. Cao, B. Zhang, H. J. Fan, S. Guo, *Adv. Sci*. **2023**, n/a, 2305806.

[19] P. Huang, H. Ying, S. Zhang, Z. Zhang, W.-Q. Han, *Adv. Energy Mater*. **2022**, 12, 2202052.

[20] Y. Li, H. Shao, Z. Lin, J. Lu, L. Liu, B. Duployer, P. O. Å. Persson, P. Eklund, L. Hultman, M. Li, K. Chen, X.-H. Zha, S. Du, P. Rozier, Z. Chai, E. Raymundo-Piñero, P.-L. Taberna, P. Simon, Q. Huang, *Nat. Mater*. **2020**, 19, 894.

[21] L. Luo, J. Song, L. Song, H. Zhang, Y. Bi, L. Liu, L. Yin, F. Wang, G. Wang, *Nano-Micro Lett.* **2019**, 11, 63.

[22] J. Gu, Q. Zhu, Y. Shi, H. Chen, D. Zhang, Z. Du, S. Yang, *ACS Nano* **2020**, 14, 891.

[23] D.-H. Nam, T.-H. Kim, K.-S. Hong, H.-S. Kwon, *ACS Nano* **2014**, 8, 11824.

[24] Z. Cao, H. Zhang, B. Song, D. Xiong, S. Tao, W. Deng, J. Hu, H. Hou, G. Zou, X. Ji, *Adv. Funct. Mater*. **2023**, 33, 2300339.

[25] a) R. Chen, C. Yang, W. Cai, H.-Y. Wang, J. Miao, L. Zhang, S. Chen, B. Liu, *ACS Energy Lett.* **2017**, 2, 1070; b) J. H. Park, C. Choi, J. B. Park, S. Yu, D.-W. Kim, *Adv. Energy Mater*. **2023**, n/a, 2302493.

[26] H. Yang, Y. Qiao, Z. Chang, H. Deng, P. He, H. Zhou, *Adv. Mater*. **2020**, 32, 2004240.

[27] L. Sun, Y. Wang, G. Duan, B. Luo, S. Zheng, J. Huang, Z. Ye, *J. Mater. Chem. A* **2023**, 11, 17188.

[28] Z. Huang, J.-C. Lai, S.-L. Liao, Z. Yu, Y. Chen, W. Yu, H. Gong, X. Gao, Y. Yang, J. Qin, Y. Cui, Z. Bao, *Nat. Energy* **2023**, 8, 577.

[29] X. Zhang, J. Li, D. Liu, M. Liu, T. Zhou, K. Qi, L. Shi, Y. Zhu, Y. Qian, *Energy Environ. Sci*. **2021**, 14, 3120.

[30] J. Gu, Y. Tao, H. Chen, Z. Cao, Y. Zhang, Z. Du, Y. Cui, S. Yang, *Adv. Energy Mater*. **2022**, 12, 2200115.

[31] Y. Wang, Z. Deng, B. Luo, G. Duan, S. Zheng, L. Sun, Z. Ye, J. Lu, J. Huang, Y. Lu, *Adv. Funct. Mater*. **2022**, 32, 2209028.

[32] B. Li, S. Liu, Y. Geng, C. Mao, L. Dai, L. Wang, S. C. Jun, B. Lu, Z. He, J. Zhou, *Adv. Funct. Mater*. **2023**, n/a, 2214033.

[33] H. Liu, J.-G. Wang, W. Hua, L. Ren, H. Sun, Z. Hou, Y. Huyan, Y. Cao, C. Wei, F. Kang, *Energy Environ. Sci*. **2022**, 15, 1872.

[34] a) R. Soni, J. B. Robinson, P. R. Shearing, D. J. L. Brett, A. J. E. Rettie, T. S. Miller, *Energy Storage Mater*. **2022**, 51, 97; b) Y. Dai, C. Zhang, W. Zhang, L. Cui, C. Ye, X. Hong, J. Li, R. Chen, W. Zong, X. Gao, J. Zhu, P. Jiang, Q. An, D. J. L. Brett, I. P. Parkin, G. He, L. Mai, *Angew. Chem., Int. Ed*. **2023**, 62, e202301192.

[35] W. Zhang, Y. Dai, R. Chen, Z. Xu, J. Li, W. Zong, H. Li, Z. Li, Z. Zhang, J. Zhu, F. Guo, X. Gao, Z. Du, J. Chen, T. Wang, G. He, I. P. Parkin, *Angew. Chem., Int. Ed*. **2023**, 62, e202212695.

[36] P. Wang, S. Liang, C. Chen, X. Xie, J. Chen, Z. Liu, Y. Tang, B. Lu, J. Zhou, *Adv. Mater*.

2022, 34, 2202733.

[37] C. Deng, X. Xie, J. Han, B. Lu, S. Liang, J. Zhou, *Adv. Funct. Mater*. **2021**, 31, 2103227.

[38] B. Yong, D. Ma, Y. Wang, H. Mi, C. He, P. Zhang, *Adv. Energy Mater*. **2020**, 10, 2002354.

[39] H. Li, Z. Wang, L. Dang, K. Yu, R. Yang, A. Fu, X. Liu, Y.-G. Guo, H. Li, *Small* **2023**, n/a, 2307722.

[40] N. Zhang, M. Jia, Y. Dong, Y. Wang, J. Xu, Y. Liu, L. Jiao, F. Cheng, *Adv. Funct. Mater*. **2019**, 29, 1807331.

[41] H. Gan, J. Wu, R. Li, B. Huang, H. Liu, *Energy Storage Mater.* **2022**, 47, 602.